Article

# Energy-Level Alignment and Orbital-Selective Femtosecond Charge Transfer Dynamics of Redox-Active Molecules on Au, Ag, and Pt Metal Surfaces

Ziyu Zhang,[¶] Liang Cao,[¶] Xue Chen, Damien Thompson,* Dongchen Qi,* and Christian A. Nijhuis*

Read Online

ACCESS | Metrics & More | Article Recommendations | SI Supporting Information

**ABSTRACT:** Charge transfer (CT) dynamics across metal−molecule interfaces has important implications for performance and function of molecular electronic devices. CT times, on the order of femtoseconds, can be precisely measured using synchrotron-based core-hole clock (CHC) spectroscopy, but little is known about the impact on CT times of the metal work function and the bond dipole created by metals and the anchoring group. To address this, here we measure CT dynamics across self-assembled monolayers bound by thiolate anchoring groups to Ag, Au, and Pt. The molecules have a terminal ferrocene (Fc) group connected by varying numbers of methylene units to a diphenylacetylene (DPA) wire. CT times measured using CHC with resonant photoemission spectroscopy (RPES) show that conjugated DPA wires conduct electricity faster than aliphatic carbon wires of a similar length. Shorter methylene connectors exhibit increased conjugation between Fc and DPA, facilitating CT by providing greater orbital mixing. We find nearly 10-fold increase in the CT time on Pt compared to Ag due to a larger bond dipole generated by partial electron transfer from the metal−sulfur bond to the carbon−sulfur bond, which creates an electrostatic field that impedes CT from the molecules. By fitting the RPES signal, we distinguish electrons coming from the Fe center and from cyclopentadienyl (Cp) rings. The latter shows faster CT rates because of the delocalized Cp orbitals. Our study demonstrates the fine tuning of CT rates across junctions by careful engineering of several parts of the molecule and the molecule−metal interface.
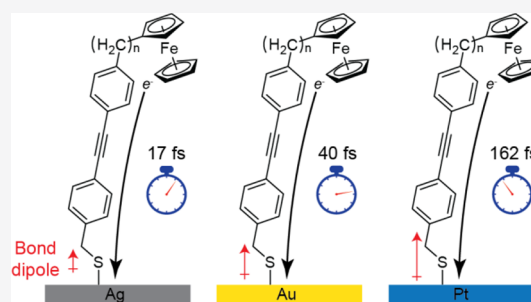
## INTRODUCTION

Rational design of molecular electronic devices with a single molecule or multimolecule assembly as the active component requires fundamental knowledge of the charge transfer (CT) pathways and mechanisms by which charge carriers move through the molecules and between the molecules and the metal electrodes that support them. A large number of different types of molecular junctions have been reported,[1] which can be broadly divided into two classes: one that utilizes self-assembled monolayers (SAMs) sandwiched between two electrodes[2] and the other that utilizes single molecules bridging two electrodes.[3] Measurements on large-area junctions based on SAMs have revealed detailed CT mechanisms,[4−6] and inspired, for instance, the design of molecular diodes and memories,[7−12] and the first large-area junctions are commercially available.[13] In this context, it is important to understand the timescales of the CT dynamics at the molecule−metal interfaces and to identify which molecular orbitals are involved in CT and how it is affected by interface dipoles. However, this information cannot be extracted from experimental CT data obtained from molecular junctions. Therefore, it is a common practice to resort to theories that rely on a series of assumptions that is very difficult or impossible to verify experimentally. Here, we report the orbital-selective CT

dynamics of a metal−molecule interface with femtosecond resolution. We study CT across molecular wires (diphenylacetylene, DPA) tethered to a redox-active moiety (Fc = ferrocene) as a function of the type of metal electrode M = Ag, Au, and Pt and tether length $(CH_2)_{n = 0−3}$. Charges injected into low-lying empty Fc orbitals LUMO+1 and LUMO+2 (LUMO = lowest unoccupied molecular orbital) decay along the DPA wire to the metal substrate, where the LUMO is centered on the DPA unit. We derive the following conclusions: the decay process slows down by a factor of 10 with increasing interface dipole, the decay rate of LUMO+1 is much more sensitive than LUMO+2 to interface dipoles, and LUMO+1 and LUMO+2 are affected differently due to their Fe and Cp characters, respectively, where $Fc = FeCp_2$ and Cp = cyclopentadienyl. These results clarify the impact of the metal electrodes on the CT dynamics involving low-lying unoccupied levels and elucidate which orbitals are involved

and how they are affected by the interface dipoles, which helps to guide future experimental and computational studies.

The CT characteristics of individual molecules and their ordered assemblies on a solid substrate have been routinely studied by the measurement of static electric conductance, implemented with a large variety of experimental techniques including break junctions,[14] junctions with carbon-based electrodes,[15−17] and liquid metals[18−20] or conductive polymers[21] as top electrodes. However, direct quantitative measurement of CT is not possible using static electrical probes, and so knowledge of the CT times along the molecules and their electrical contacts is lacking, which limits the understanding and impedes the optimization of molecular electronic devices. Synchrotron-based core-hole clock (CHC) spectroscopy provides a means of measuring the time scale of the CT dynamics across the metal−molecule interface selectively for each relevant molecular orbital. Figure 1
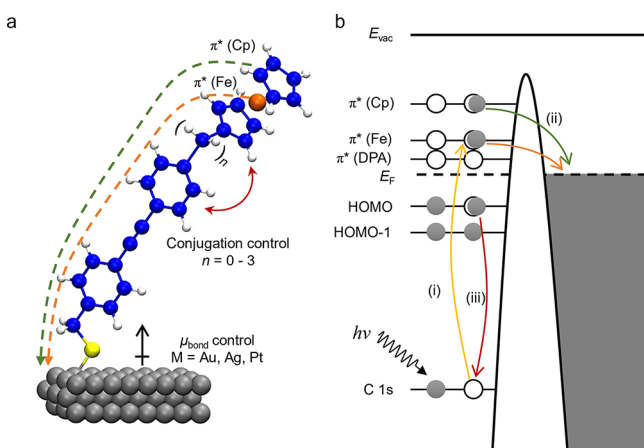


**Figure 1.** (a) Schematic representation of the SAM structure of M−S−CH$_2$−Ph−CC−Ph−(CH$_2$)$_n$−Fc where M = Ag, Au, and Pt and $n$ = 0−3. The red double arrow indicates electronic coupling between Fc and DPA. The dashed orange and green arrows represent the CT from $\pi$*(Fe) and $\pi$*(Cp), respectively. (b) Energy level diagram for the interfacial CT from Fc to the metal substrate. Radiation $h\nu$ denotes the photon that excites core electrons in the molecule into unoccupied molecular orbitals, leaving behind a core hole as depicted by the yellow arrow (i); excited electron transfer from a molecule to a metal (ii) from two hybridized orbitals dominated by a cyclopentadienyl (Cp, green) group or central Fe (orange); $E_F$ is the Fermi level; normal Auger decay of an electron from the highest occupied molecular orbital (HOMO) down into the buried core-hole C 1s level is marked by the red arrow (iii). The energy level of the $\pi$*(DPA) LUMO is also marked for reference.

shows the electronic processes involved in the CHC measurement. We describe below the essential features of the measurement; for a detailed account of the principles of CHC spectroscopy and the estimation of CT times using the CHC technique, readers are referred to comprehensive reviews.[22−25]

A core electron is photoexcited to the unoccupied molecular orbitals, generating a core hole. The core-hole lifetime acts as an internal reference clock to time the CT dynamics. Within this period, the core hole can decay through the process of participator decay (resonant photoemission involving the photoexcited electron in the low-lying unoccupied molecular energy levels) and/or spectator decay (resonant Auger intramolecular electron transfer in response to the presence

of the photoexcited electron), leading to the enhancement of photoelectron signals. When the unoccupied orbitals of the molecules couple with the continuum electronic states of the metal surface, the excited electron gets transferred to the metal. The participator and/or spectator decays will be quenched and the core hole decays through the nonresonant and regular Auger processes. From the extent of this quenching effect, we can determine the time of the CT. The CHC technique is element-, site-, and orbital-specific, allowing selective studies of CT dynamics of elements and/or orbitals of interest at the time scales of subfemtoseconds to a few hundreds of femtoseconds.[23,26] In particular, the CHC technique's ability to distinguish electrons coming from different molecular orbitals makes it an ideal tool to study junctions built from complex molecules that may involve multiple tunneling pathways, and CHC is an ideal spectroscopic benchmark for density functional theory (DFT) calculations of the electronic structure of molecular tunnel junctions.

The CHC technique has been used to study a variety of metal−molecule and metal−semiconductor interfaces.[27−29] In the context of SAMs, it has been used to investigate the effect of molecular conformation,[30−32] molecular dipoles,[33,34] and molecular anchoring groups[35] on the CT rate. Comparatively little is known about the impact on the CT dynamics of the work function of the metal and associated metal−molecule bonds that depend heavily on the type of the metal used (in particular, bond dipole or push back effects).[36] It is well known that the interface dipole, which consists of the bond dipole and the molecular dipole, can affect the work function of the electrodes, $\Phi_m$, and hence modulate the barrier height for electron or hole injection given by eq 1.[37,38]

$$\Delta\Phi_m = \frac{eN}{\varepsilon\varepsilon_0} \times (\mu_{bond} + \mu_{mol})$$

(1)

where $\mu_{bond}$ is the bond dipole associated with the metal−sulfur bond and $\mu_{mol}$ is the molecular dipole, $e$ is the electron charge, $N$ is the number of molecules per unit of area (which directly relates to the surface coverage), $\varepsilon$ is the dielectric constant in the junction, and $\varepsilon_0$ is the permittivity of free space. In large-area molecular junctions based on SAMs, $\mu_{bond}$ has a large influence on the electronic properties of these devices.[39,40] For instance, Frisbie et al. reported that increasing the interface dipole results in increasing molecule−electrode contact resistances, but they have also reported the opposite trend. More specifically, they reported that for SAMs of S−(CH$_2$)$_{n-1}$CH$_3$ or S−(Ph)$_n$ (Ph = phenyl), the contact resistance of molecular junctions decreases with increasing $\Phi_m$ of the native metal electrode (i.e., $\Phi_{Ag}$ = 4.5 eV, $\Phi_{Au}$ = 5.2 eV, and $\Phi_{Pt}$ = 5.7 eV) where CT is dominated by the HOMO[41,42] and observed the opposite trend for a SAM of perylene diimide where CT is dominated by the LUMO.[43] In these studies, the conclusions were drawn by fitting the CT data to a single-level Landauer theory, and the relevant orbitals were identified based on DFT calculations of the molecules in the gas phase, without the molecule−metal interface. This approach relies on a large number of assumptions (especially on the orbitals that are involved in CT) and hence it is not possible to verify experimentally which orbitals are involved in CT and how much the tunneling rates from each orbital contributes to the overall CT process.

In this study, we clarify the effect of the metal substrates on the CT dynamics across the molecule−metal interface and identify the molecular orbitals involved in CT. We used CHC

spectroscopy to investigate the CT time in SAMs of $M-S-CH_2-Ph-CC-Ph-(CH_2)_n-Fc$ (M = Ag, Au, and Pt, n = 0–3). The structure of the SAM is shown in Figure 1. These molecules have multiple low-lying unoccupied $\pi^*$ orbitals on Fc and DPA units that sit above the Fermi level of the substrates, $E_F$. The excited electrons residing in these orbitals can transfer to the conduction band of the metal substrate and conjugate between Fc and DPA, which can be controlled by changing the number of $CH_2$ linker units, n, which is expected to have a significant impact on the CT time scale. The effect of both the energy level alignment near the Fermi level and the bond dipole of the metal−sulfur bonds can be determined by comparing SAMs on three different metal substrates Au, Ag, and Pt. We used the CHC method in resonant photoemission spectroscopy (RPES) to examine the CT dynamics between the Fc functional group and the metal substrate via a conjugated molecular backbone (Figure 1). To access the CT timescale, $\tau_{CT}$, from a certain orbital, we need an isolated system in which photoexcited electrons on that orbital only decay by normal Auger process and do not transfer to the substrate. We have shown, in agreement with others,[44] that three methylene units can electronically decouple Fc from the metal,[45] and thus here we assume that with n = 3, the Fc units are decoupled from the DPA backbone and behave as an isolated system. The decrease of the intensity for the coupled SAMs with n < 3 corresponds to the population of electrons transferring from the Fc units via DPA to the substrate.

We were able to measure $\tau_{CT}$ for two distinct, non-degenerate molecular frontier orbitals on the Fc group, one centered on the Cp unit (LUMO+1) and the other on the Fe atom (LUMO+2), and show how the corresponding values of $\tau_{CT}$ depend on the degree of conjugation between Fc and DPA (i.e., value of n) and the type of metal electrode, which have M−S bond dipoles following the order of Pt > Au > Ag.[46] Our results confirm that (i) conjugated molecular chains facilitate faster electron transfer compared to aliphatic chains, in agreement with the results reported for other systems,[47−49] (ii) CT time increases exponentially with tunneling distance, and (iii) the CT times for the same molecule on three different metals follow the trend of Pt > Au > Ag, quantifying how larger bond dipoles at the metal−molecule interface retard the CT process.

## ■ RESULTS AND DISCUSSION

The structure of the $M-S-CH_2-Ph-CC-Ph-(CH_2)_n-Fc$ SAMs was confirmed by X-ray photoemission spectroscopy (XPS) using our well-established protocol.[50] The sulfur 2p spectra show that they are predominantly chemisorbed, and the film thickness does not vary significantly (Figures S1−S3 and Table S1). We have previously measured the static current−voltage behavior of these SAMs with gold as the only substrate and a eutectic alloy of gallium and indium as the top electrode.[6] Here, we investigated the energy level alignment for the SAMs on the three different metals. We used ultraviolet photoemission spectroscopy (UPS) and near-edge X-ray absorption fine structure (NEXAFS) spectroscopy supported by projected density of states (PDOS) distributions obtained from DFT calculations. The results are shown in Figure 2.

The work function of the different metals differs by up to 1.2 eV, but the HOMO and LUMO energy levels of the SAM with respect to the metal Fermi level $E_F$ remain almost constant. We attribute the constant HOMO energy to Fermi level pinning.[2,51] The LUMO is located primarily at the DPA and
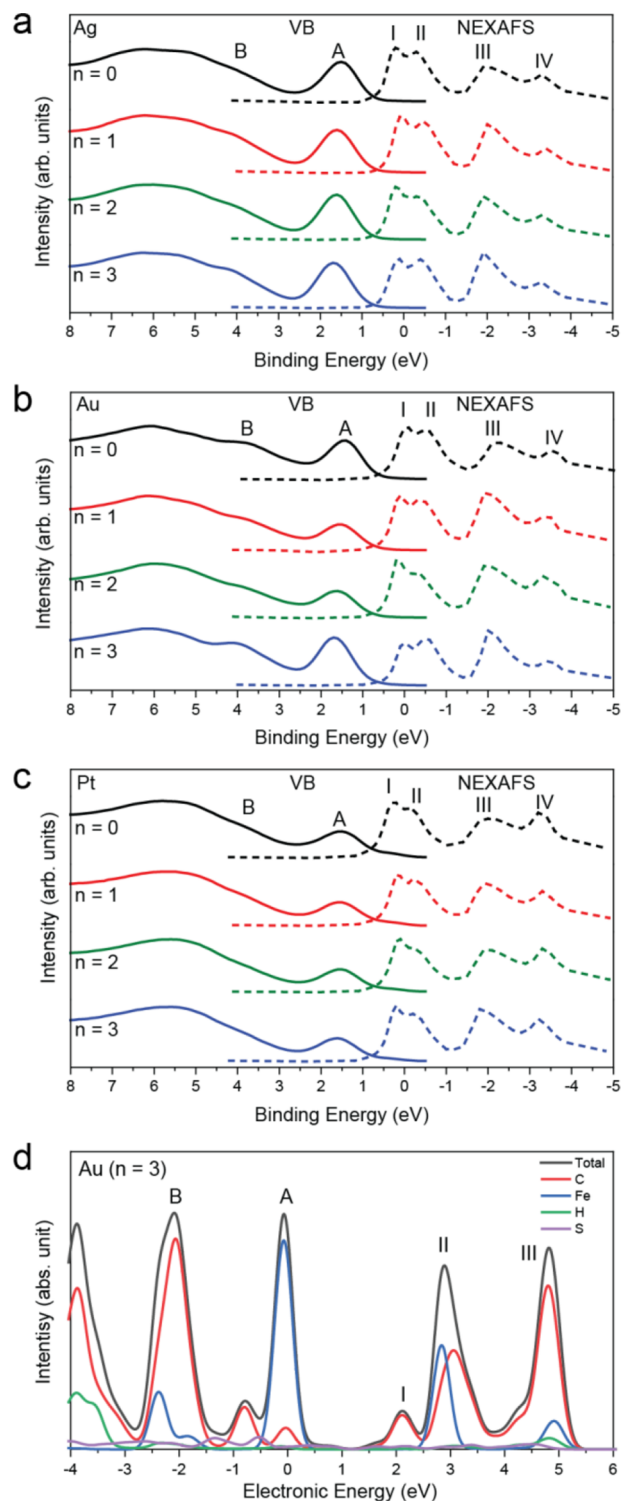


**Figure 2.** Aligned valence band (VB) spectra from UPS and the C K-edge NEXAFS spectra of the SAMs on (a) Au, (b) Ag, and (c) Pt substrates. The NEXAFS spectra were realigned to the Fermi level $E_F$ by subtracting the binding energy of the C 1s core-level peak. (d) Calculated PDOS of the $Au-S-CH_2-Ph-CC-Ph-(CH_2)_3-Fc$ SAM with the Fermi level set to zero. The full data set for all metals and n values is shown in Figures S8−S10.

the Cp rings in Fc, and therefore, is not affected by the metal−sulfur bonds. To understand the contribution of molecular orbitals to features close to $E_F$, DFT calculations were performed to map the projected (or partial) DOS (PDOS,
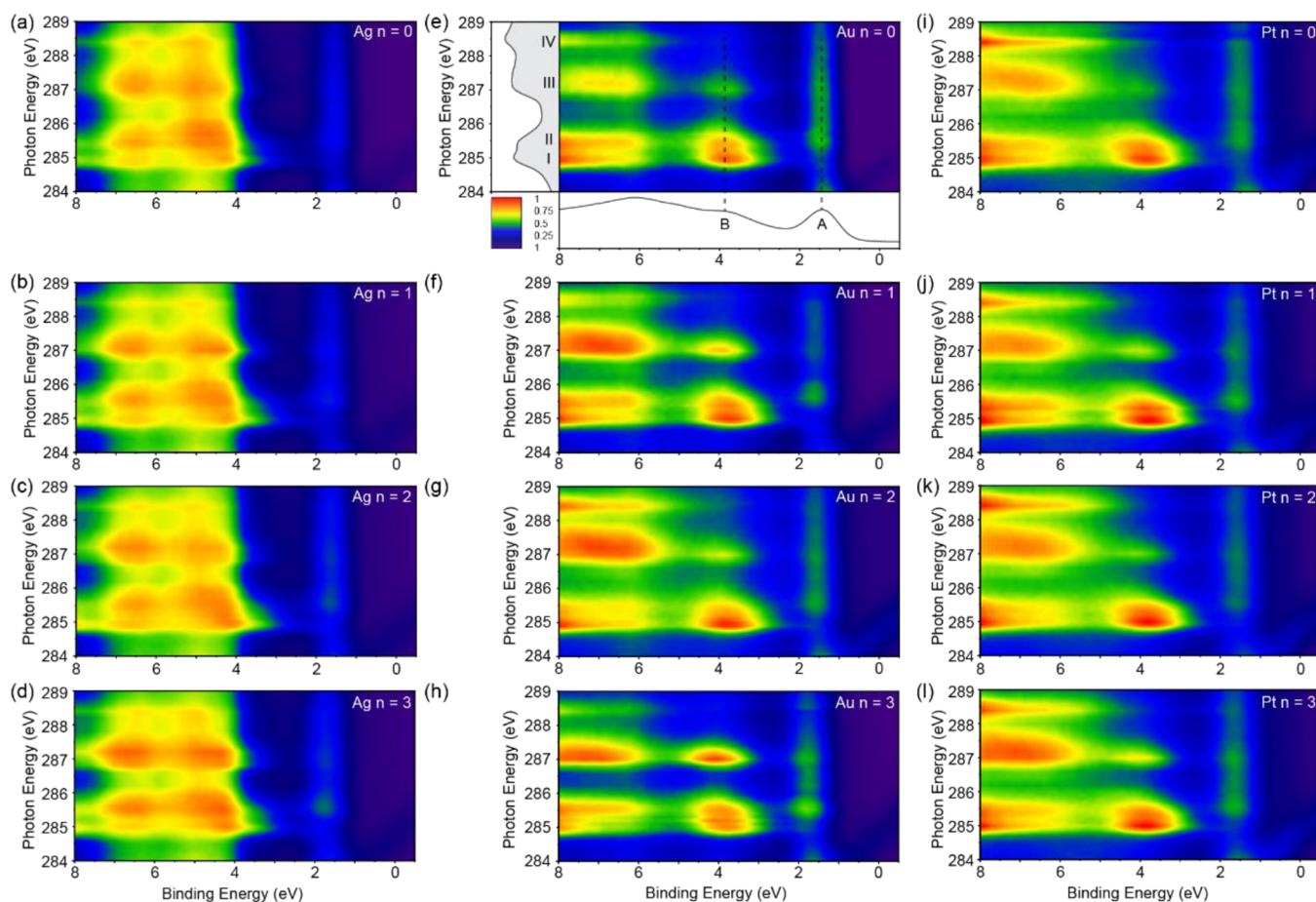
**Figure 3.** RPES contour plots for SAMs of M−S−CH$_2$−Ph−CC−Ph−(CH$_2$)$_n$−Fc. (a−d) M = Ag, (e−h) M = Au, and (i−l) M = Pt, with subpanels from top to bottom showing $n$ = 0 to $n$ = 3. The corresponding UPS and NEXAFS spectra are shown in panel (e) to highlight the resonant-enhanced features.

Figure 2d). Peak A in the VB spectra corresponds to the HOMO of the molecules, which consists of the Fe 3d$_{z^2}$ and Fe 3d$_{xy}$ orbitals with a minor contribution from central C≡C in the DPA wire (see orbital-projected DOS distributions and computed electron density surfaces in the Supporting Information Figures S11−S13). The small 0.1−0.2 eV shift of the HOMO energy (peak A) toward higher binding energies with increasing molecular length is likely caused by photohole screening effects, which is commonly observed in monolayers.[52−54] Peak B mainly consists of π orbitals in the Cp rings and DPA. We attribute the changes in the intensity of peak B to differences in the DOS of the metal surfaces. For instance, Pt has the largest signals around $E_F$ and overwhelms the molecule features.[55] The DFT calculations show that the NEXAFS peak I (the LUMO) has no contribution from Fc and can be attributed to the transition from C 1s to a π* antibonding level delocalized along the DPA wire. Peak II (the LUMO+1) corresponds to a transition to the orbitals of Fe 3d$_{xz}$ and Fe 3d$_{yz}$ hybridized with the Cp rings, with contribution also from π* of the DPA phenyl rings (see Cp and DPA PDOS shown in Figure S11 and the corresponding electron density surfaces shown in Figure S13). Peak III (the LUMO+2) represents a transition to π* of Cp rings hybridized with the Fe 3d$_{xy}$ orbital. The PDOS shows the contributions to peak III of 78, 17, 3, and 2% for C, Fe, H, and S, with 85% of the carbon contribution on Cp and 71% of the Fe contribution on 3d$_{xy}$ (Figures S11 and S12). Peak IV originates from the

transition to σ* of the C−H/C−S bonds, as discussed in our earlier NEXAFS results of Au−S(CH$_2$)$_{11}$Fc SAMs.[56] The peak assignments from the periodic DFT molecule−metal calculations are generally consistent with previous assignments from gas-phase models of S−(CH$_2$)$_n$−Fc−(CH$_2$)$_{13-n}$ molecules bound to a single Au metal atom used in our previous study.[57]

Figure 3 shows the RPES contour plots for the SAMs with $n$ = 0, 1, or 3 on the three metal substrates. The resonantly enhanced VB region features between 0 and 8 eV (peaks A and B) are clearly visible at photon energies of 284.8−285.1, 285.2−286.2, 286.8−287.5, and 288.3−288.6 eV, corresponding to the resonances I, II, III, and IV in NEXAFS spectra. The features at higher binding energies (>8 eV) are dominated by normal Auger decay signals from lower-lying levels and are omitted here for clarity. Resonant enhancement patterns are sharper for SAMs on Au (Figure 3e−h) and Pt (Figure 3i−l) than on Ag (Figure 3a−d), which may be due to the strong Ag 4d signals that overwhelm resonant signals or could also be due to ultrafast CT between Fc and Ag (see below).

The resonant enhancement of a specific peak is strong when the corresponding valence states have a spatial overlap with the unoccupied orbitals that the core electrons are excited into. Figure 3 shows that the signal for peak A (HOMO) is strongly enhanced for photon energies corresponding to mainly resonances II and III (see Figure 3e for a guide to the eye), with peak A and resonances II and III featuring strong contributions from the iron center. On the other hand, peak A
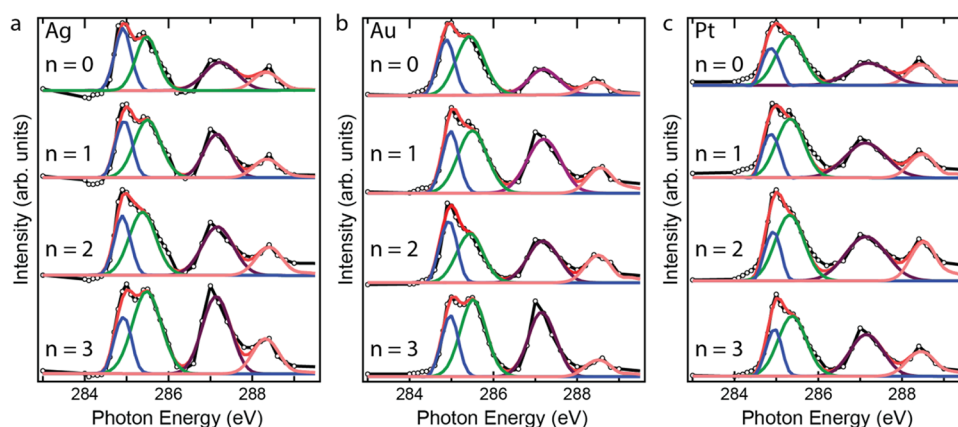
**Figure 4.** Integrated RPES spectra for SAMs of M−S−CH$_2$−Ph−CC−Ph−(CH$_2$)$_n$−Fc and the corresponding fitting curves. Metal substrate is (a) Ag, (b) Au, and (c) Pt. The intensity for each photon energy is the integral of VB spectra in the binding energy range of 0 to 7 eV. The fitted peak denotes resonances I (blue), II (green), III (purple), and IV (pink).

is weakly enhanced for the transition to the occupied orbitals on the DPA rings (in particular, resonance I). In contrast, peak B is strongly enhanced for resonance I and to a lesser extent for resonance II and then III, confirming the contribution from the DPA unit, which agrees well with the computed electronic structures. To quantify the CT times from the SAMs to the different metal substrates, the integrated RPES profiles were obtained by integrating the resonant photoemission signals (i.e., participator decay) in the RPES spectra within the binding energy window between 0 and 7 eV and are plotted as a function of photon energy as shown in Figure 4.

To allow for a direct comparison of intensities, the C K-edge NEXAFS spectra were obtained by integrating signals over the entire binding energy window of 0−20 eV. The NEXAFS spectra represent the total cross section of electron excitation, whereas the RPES profile receives contributions mainly from resonant decay; their relative ratio counts the population of electrons undergoing participator decay, which in turn allows calculation of CT times. To extract the accurate intensity of each resonance, the least-squares peak fitting was performed for both spectra (Figure 4 and Figure S7, with details of the fitting procedure given in the Supporting Information). The calculated $\tau_{CT}$ values for resonances II and III associated with Fc moieties are summarized in Table 1 and plotted in Figure 5. For SAMs on Pt, the $I_{RPES}/I_{NEXAFS}$ values for $n = 1$ and 2 are comparable with that for $n = 3$ within the uncertainty of the signals, indicating relatively long CT times ($\gg$200 fs) beyond the range accessible by the CHC technique. Therefore, we are
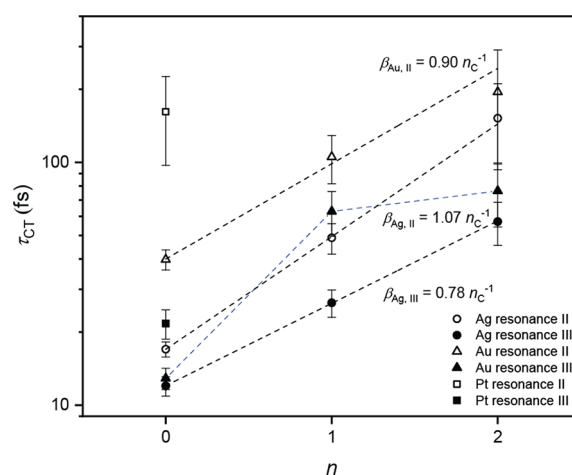


**Figure 5.** CT time scale from resonances II (open) and III (solid) to the metal surfaces Ag (circle), Au (triangle), and Pt (square) as a function of the number of CH$_2$ groups ($n$) between Fc and DPA. The black dashed lines represent the best linear fits for the experimental data (in log scale). The blue dashed line connects the data points for resonance III on Au, which does not follow an exponential decay. The $\beta$ values derived from the fittings are shown.

only able to provide a lower limit of these lifetimes of 200 fs in Table 1.

The most obvious results from the data shown in Table 1 and Figure 5 are that the conjugated DPA wire allows for much faster CT compared to an aliphatic linker. In our previous study on Au−S−(CH$_2$)$_n$−Fc−(CH$_2$)$_{13-n}$ SAMs,[57] the CT times were already too long to be detected by CHC spectroscopy when $n = 5$ (tunneling distance = 7.3 Å). In the present SAM, the distance from Fc to Au is more than twice this distance, 15.9 Å, for $n = 0$ (as measured by XPS, Table S1) but the CT time is only 12.9 ± 1.3 fs. This is due to conjugated linkers providing better orbital delocalization for resonances II and III on Fc, which accelerates the transfer of the excited electron to the metal conduction band via off-resonant tunneling involving the LUMO delocalized over the DPA unit. On all metal surfaces, the CT times for resonance III are shorter than those for resonance II ($\tau_{II} > \tau_{III}$), which can also be explained by delocalization. Cao et al. showed that the electrons excited to unoccupied orbitals with mostly Fe 3d character (resonance II) remain localized on Fc.[57] On the

**Table 1. Charge Transfer Times ($\tau_{CT}$)$^a$ from the LUMO+1 (Peak II) and LUMO+2 (Peak III) to the Metal Surfaces$^b$**

| metal | resonance | $\tau_{CT}$ (fs) | | |
| --- | --- | --- | --- | --- |
| | | $n = 0$ | $n = 1$ | $n = 2$ |
| Ag | II | 17.0 ± 1.2 | 48.9 ± 7.0 | 152.0 ± 58.8 |
| | III | 12.0 ± 1.1 | 26.4 ± 3.4 | 57.0 ± 11.5 |
| Au | II | 39.8 ± 3.8 | 105.3 ± 23.7 | 194.9 ± 95.4 |
| | III | 12.9 ± 1.3 | 62.8 ± 13.1 | 76.3 ± 22.1 |
| Pt | II | 161.6 ± 64.4 | $\gg$200 | $\gg$200 |
| | III | 21.7 ± 3.0 | $\gg$200 | $\gg$200 |

$^a$Obtained from the intensity ratio $I_{RPES}/I_{NEXAFS}$ as explained in the text. $^b$The error represents the standard deviation of the fitting residual for each resonance.

other hand, electrons residing in the much more delocalized Cp $\pi^*$ orbitals (resonance III) provide a faster and more efficient CT channel (see also DFT surfaces in Figure S13). Hot electron relaxation from LUMO+2 to LUMO+1 could also shorten the apparent CT times for resonance III. This relaxation process, however, occurs on the order of picoseconds,[58] which is too slow to interfere with our experiments. In addition, this effect would also be present in the reference system ($n$ = 3) and therefore should not affect the results.

In analogy to tunneling currents in molecular junctions where the tunneling currents decay exponentially with a tunneling decay constant $\beta$, we expect the CT times to exponentially increase with $d$. The relationship between CT time ($\tau_{CT}$, through a hydrocarbon molecular wire to an electrode) and the tunneling distance $d$ can be described as[44,59]

$$\tau_{CT} = \tau_0 e^{\beta d}$$

where $\tau_0$ is the pre-exponential factor. For a specific resonance, the CT times increase with increasing number of $CH_2$ groups. The $\beta$ values for tunneling current in alkane-based molecular junctions have been reported for multiple testbeds and their values are 0.8−1.1 $n^{-1}$ ($n$ = number of carbons).[60,61] Junctions with molecules with conjugated backbones have much lower $\beta$ values in the range of 0.2−0.5 $n^{-1}$. The fitting results shown in Figure 5 show that for resonance II, both Ag and Au give $\beta$ values close to their static analogue ($\beta_{Ag,II}$ = 1.07 $n^{-1}$, $\beta_{Au,II}$ = 0.90 $n^{-1}$) of aliphatic molecules. Resonance III on Ag gives a $\beta$ value of 0.78 $n^{-1}$ that is considerably smaller than that of resonance II. Surprisingly, on Au, resonance III does not follow a clear exponential decay for unclear reasons. This result shows that even though in CHC we study the CT from the excited states of molecules to one substrate as opposed to CT through molecules between two electrodes, the mechanism of CT still shares the same characteristics and with CHC we can identify which discrete orbital dominates the through-bond tunneling process (resonance II in this case). Zharnikov also observed an exponential decay of CT time with increasing length of alkyl chains in SAMs of Au−S−$(CH_2)_n$−CN.[62] However, when the orbital participating in the transfer/transport is highly delocalized (resonance III), the CT rate decay does not behave in the same way as the static current and CT can be highly efficient. In molecular junctions, however, normally the applied voltage is low (to avoid electrical breakdown) and therefore tunneling in a molecular junction does not involve such high-lying orbitals (such as LUMO+2 for resonance III reported here) although they potentially are much more efficient in CT than the lower-energy orbitals.

When comparing the influence of substrates on the CT times, $\tau(Pt) > \tau(Au) > \tau(Ag)$ is found for both resonance II and resonance III, for SAMs with a given $n$ value. This result indicates that the "contact resistance" is the largest for SAMs on Pt and the lowest for those SAMs on Ag. Although the overall interface dipole can be determined with UPS,[63] the contributions of $\mu_{bond}$ and $\mu_{mol}$ cannot be separated by photoemission spectroscopy methods. DFT calculations of the charge density redistribution on the interfaces can precisely access $\mu_{bond}$, which is reported to follow the trend Ag < Au < Pt.[39,64] Larger bond dipoles give rise to lower contact resistances when the CT is mediated by the HOMO orbital of the molecule, as shown by the measurement of static electric conductance in several SAM-based junctions.[41,42,65] On the other hand, LUMO-assisted CT has higher contact resistances with increasing bond dipoles.[49] In this CHC study, electrons transfer from the LUMO+1 and LUMO+2 of the molecules to the metals and our results agree with the observations in ref 43. The d or s bands of the metals have been reported to affect CT rates across metal−molecule interfaces in the case of Cu electrodes.[66] We did not see this effect in our system because no significant differences were found in the full DOS for the SAMs on different metals or for the metal signal for molecule−metal versus reference bare metal models for any of the metals. More detailed studies designed to reveal the possible role of the band structure of the metal on the CT rates will be an interesting future direction.

## CONCLUSIONS

We investigated the femtosecond-scale CT dynamics between two molecular orbitals on Fc-functionalized molecules and three metal surfaces by CHC spectroscopy. We demonstrated that the RPES−CHC approach allows us to distinguish the contributions from resonances II and III, which come from different orbitals in the molecule. We have identified three important design rules for controlling CT in these types of molecular junctions. First, conjugation between Fc and DPA plays an important role in facilitating the CT through the molecules, where a single $CH_2$ group insertion is sufficient to reduce the conjugation and dramatically retard the CT process. Second, the metal−sulfur bond dipoles create an additional barrier, resulting in longer CT times for metals with larger bond dipoles. Finally, strongly localized molecular orbitals with a predominantly Fe 3d character show slower CT than molecular orbitals that are more delocalized on Fc. In general, this study shows how the speed of CT between a molecule and a metal surface can be controlled by rationally engineering the structure of the molecules themselves in tandem with the metal−molecule bond chemistry.

## EXPERIMENTAL SECTION

A detailed description of the synthesis of the monolayer precursors is given in ref 6. All other experimental procedures follow previously reported methods and are described in the Supporting Information: preparation of the metal surfaces and formation of SAMs (Section S1), experimental details (Section S2) and analysis (Section S3) of the RPES and NEXAF measurements, and all details regarding the DFT calculations (Section S4).

## ASSOCIATED CONTENT

### Ⓢ Supporting Information

The Supporting Information is available free of charge at https://pubs.acs.org/doi/10.1021/acs.jpcc.1c04655.

Material and methods for fabrication of the samples; photoemission spectroscopy; details of fitting of the RPES and NEXAFS spectra; and details of DFT calculations (PDF)

## AUTHOR INFORMATION

### Corresponding Authors

**Damien Thompson** − *Department of Physics, Bernal Institute, University of Limerick, Limerick V94 T9PX, Ireland;* ⓞ orcid.org/0000-0003-2340-5441; Email: Damien.Thompson@ui.ie

**Dongchen Qi** − *Centre for Materials Science, School of Chemistry and Physics, Queensland University of Technology,*

Brisbane, Queensland 4001, Australia; orcid.org/0000-0001-8466-0257; Email: dongchen.qi@qut.edu.au

Christian A. Nijhuis − Department of Chemistry, National University of Singapore, 117543, Singapore; Centre for Advanced 2D Materials, National University of Singapore, Singapore 117546, Singapore; Hybrid Materials for Opto-Electronics Group, Department of Molecules and Materials, MESA+ Institute for Nanotechnology and Center for Brain-Inspired Nano Systems, Faculty of Science and Technology, University of Twente, 7500 AE Enschede, The Netherlands; orcid.org/0000-0003-3435-4600; Email: c.a.nijhuis@utwente.nl

### Authors

Ziyu Zhang − Department of Chemistry, National University of Singapore, 117543, Singapore

Liang Cao − Anhui Province Key Laboratory of Condensed Matter Physics at Extreme Conditions, High Magnetic Field Laboratory, Chinese Academy of Sciences, Hefei, Anhui 230031, China; orcid.org/0000-0001-7453-7060

Xue Chen − Anhui Province Key Laboratory of Condensed Matter Physics at Extreme Conditions, High Magnetic Field Laboratory, Chinese Academy of Sciences, Hefei, Anhui 230031, China

Complete contact information is available at:
https://pubs.acs.org/10.1021/acs.jpcc.1c04655

### Author Contributions

¶Z.Z. and L.C. contributed equally.

### Notes

The authors declare no competing financial interest.

## ■ REFERENCES

(1) Jeong, H.; Kim, D.; Xiang, D.; Lee, T. High-Yield Functional Molecular Electronic Devices. ACS Nano 2017, 11, 6511−6548.

(2) Vilan, A.; Aswal, D.; Cahen, D. Large-Area, Ensemble Molecular Electronics: Motivation and Challenges. Chem. Rev. 2017, 117, 4248−4286.

(3) Xin, N.; Guan, J.; Zhou, C.; Chen, X.; Gu, C.; Li, Y.; Ratner, M. A.; Nitzan, A.; Stoddart, J. F.; Guo, X. Concepts in the Design and Engineering of Single-Molecule Electronic Devices. Nat. Rev. Phys. 2019, 1, 211−230.

(4) Yan, H.; Bergren, A. J.; McCreery, R.; Della Rocca, M. L.; Martin, P.; Lafarge, P.; Lacroix, J. C. Activationless Charge Transport across 4.5 to 22 Nm in Molecular Electronic Junctions. Proc. Natl. Acad. Sci. 2013, 110, 5326−5330.

(5) Nguyen, Q. V.; Martin, P.; Frath, D.; Della Rocca, M. L.; Lafolet, F.; Bellinck, S.; Lafarge, P.; Lacroix, J.-C. Highly Efficient Long-Range Electron Transport in a Viologen-Based Molecular Junction. J. Am. Chem. Soc. 2018, 140, 10131−10134.

(6) Yuan, L.; Wang, L.; Garrigues, A. R.; Jiang, L.; Annadata, H. V.; Anguera Antonana, M.; Barco, E.; Nijhuis, C. A. Transition from Direct to Inverted Charge Transport Marcus Regions in Molecular Junctions via Molecular Orbital Gating. Nat. Nanotechnol. 2018, 13, 322−329.

(7) Chen, X.; Roemer, M.; Yuan, L.; Du, W.; Thompson, D.; del Barco, E.; Nijhuis, C. A. Molecular Diodes with Rectification Ratios Exceeding 105 Driven by Electrostatic Interactions. Nat. Nanotechnol. 2017, 12, 797−803.

(8) Kumar, S.; Merelli, M.; Danowski, W.; Rudolf, P.; Feringa, B. L.; Chiechi, R. C. Chemical Locking in Molecular Tunneling Junctions Enables Nonvolatile Memory with Large On−Off Ratios. Adv. Mater. 2019, 31, 1807831.

(9) Han, Y.; Nickle, C.; Zhang, Z.; Astier, H. P. A. G.; Duffin, T. J.; Qi, D.; Wang, Z.; del Barco, E.; Thompson, D.; Nijhuis, C. A. Electric-Field-Driven Dual-Functional Molecular Switches in Tunnel Junctions. Nat. Mater. 2020, 19, 843−848.

(10) Qiu, X.; Rousseva, S.; Ye, G.; Hummelen, J. C.; Chiechi, R. C. In Operando Modulation of Rectification in Molecular Tunneling Junctions Comprising Reconfigurable Molecular Self-Assemblies. Adv. Mater. 2021, 33, 2006109.

(11) Hayakawa, R.; Karimi, M. A.; Wolf, J.; Huhn, T.; Zöllner, M. S.; Herrmann, C.; Scheer, E. Large Magnetoresistance in Single-Radical Molecular Junctions. Nano Lett. 2016, 16, 4960−4967.

(12) Schwarz, F.; Kastlunger, G.; Lissel, F.; Egler-Lucas, C.; Semenov, S. N.; Venkatesan, K.; Berke, H.; Stadler, R.; Lörtscher, E. Field-Induced Conductance Switching by Charge-State Alternation in Organometallic Single-Molecule Junctions. Nat. Nanotechnol. 2016, 11, 170−176.

(13) Peplow, M. Rebooting the Molecular Computer. ACS Cent. Sci. 2016, 2, 874−877.

(14) Gehring, P.; Thijssen, J. M.; van der Zant, H. S. J. Single-Molecule Quantum-Transport Phenomena in Break Junctions. Nat. Rev. Phys. 2019, 1, 381−396.

(15) Xu, Q.; Scuri, G.; Mathewson, C.; Kim, P.; Nuckolls, C.; Bouilly, D. Single Electron Transistor with Single Aromatic Ring Molecule Covalently Connected to Graphene Nanogaps. Nano Lett. 2017, 17, 5335−5341.

(16) Cao, Y.; Dong, S.; Liu, S.; Liu, Z.; Guo, X. Toward Functional Molecular Devices Based on Graphene−Molecule Junctions. Angew. Chem., Int. Ed. 2013, 52, 3906−3910.

(17) Seo, S.; Min, M.; Lee, S. M.; Lee, H. Photo-Switchable Molecular Monolayer Anchored between Highly Transparent and Flexible Graphene Electrodes. Nat. Commun. 2013, 4, 1920.

(18) Rampi, M. A.; Whitesides, G. M. A Versatile Experimental Approach for Understanding Electron Transport through Organic Materials. Chem. Phys. 2002, 281, 373−391.

(19) Chiechi, R. C.; Weiss, E. A.; Dickey, M. D.; Whitesides, G. M. Eutectic Gallium−Indium (EGaIn): A Moldable Liquid Metal for Electrical Characterization of Self-Assembled Monolayers. Angew. Chem., Int. Ed. 2008, 47, 142−144.

(20) Dickey, M. D.; Chiechi, R. C.; Larsen, R. J.; Weiss, E. A.; Weitz, D. A.; Whitesides, G. M. Eutectic Gallium-Indium (EGaIn): A Liquid Metal Alloy for the Formation of Stable Structures in Microchannels at Room Temperature. Adv. Funct. Mater. 2008, 18, 1097−1104.

(21) Neuhausen, A. B.; Hosseini, A.; Sulpizio, J. A.; Chidsey, C. E. D.; Goldhaber-Gordon, D. Molecular Junctions of Self-Assembled Monolayers with Conducting Polymer Contacts. ACS Nano 2012, 6, 9920−9931.

(22) Brühwiler, P. A.; Karis, O.; Mårtensson, N. Charge-Transfer Dynamics Studied Using Resonant Core Spectroscopies. Rev. Mod. Phys. 2002, 74, 703−740.

(23) Cao, L.; Gao, X.-Y.; Wee, A. T. S.; Qi, D.-C. Quantitative Femtosecond Charge Transfer Dynamics at Organic/Electrode Interfaces Studied by Core-Hole Clock Spectroscopy. In Synchrotron

*Radiation in Materials Science.* John Wiley & Sons, Ltd, 2018, pp. 137−178.

(24) Zharnikov, M. Femtosecond Charge Transfer Dynamics in Monomolecular Films in the Context of Molecular Electronics. *Acc. Chem. Res.* **2020**, *53*, 2975−2984.

(25) Besley, N. A. Modeling of the Spectroscopy of Core Electrons with Density Functional Theory. *WIREs Comput. Mol. Sci.* **2021**, *11*, e1527.

(26) Föhlisch, A.; Feulner, P.; Hennies, F.; Fink, A.; Menzel, D.; Sanchez-Portal, D.; Echenique, P. M.; Wurth, W. Direct Observation of Electron Dynamics in the Attosecond Domain. *Nature* **2005**, *436*, 373−376.

(27) Vilmercati, P.; Cvetko, D.; Cossaro, A.; Morgante, A. Heterostructured Organic Interfaces Probed by Resonant Photo-emission. *Surf. Sci.* **2009**, *603*, 1542−1556.

(28) Friedlein, R.; Braun, S.; de Jong, M. P.; Osikowicz, W.; Fahlman, M.; Salaneck, W. R. Ultra-Fast Charge Transfer in Organic Electronic Materials and at Hybrid Interfaces Studied Using the Core-Hole Clock Technique. *J. Electron Spectrosc. Relat. Phenom.* **2011**, *183*, 101−106.

(29) Eads, C. N.; Bandak, D.; Neupane, M. R.; Nordlund, D.; Monti, O. L. A. Anisotropic Attosecond Charge Carrier Dynamics and Layer Decoupling in Quasi-2D Layered SnS 2. *Nat. Commun.* **2017**, *8*, 1369.

(30) Wang, L.; Liu, L.; Chen, W.; Feng, Y.; Wee, A. T. S. Configuration-Dependent Interface Charge Transfer at a Molecule−Metal Junction. *J. Am. Chem. Soc.* **2006**, *128*, 8003−8007.

(31) Kladnik, G.; Puppin, M.; Coreno, M.; de Simone, M.; Floreano, L.; Verdini, A.; Morgante, A.; Cvetko, D.; Cossaro, A. Ultrafast Charge Transfer Pathways Through A Prototype Amino-Carboxylic Molecular Junction. *Nano Lett.* **2016**, *16*, 1955−1959.

(32) Batra, A.; Kladnik, G.; Vázquez, H.; Meisner, J. S.; Floreano, L.; Nuckolls, C.; Cvetko, D.; Morgante, A.; Venkataraman, L. Quantifying Through-Space Charge Transfer Dynamics in π-Coupled Molecular Systems. *Nat. Commun.* **2012**, *3*, 1086.

(33) Werner, P.; Wächter, T.; Asyuda, A.; Wiesner, A.; Kind, M.; Bolte, M.; Weinhardt, L.; Terfort, A.; Zharnikov, M. Electron Transfer Dynamics and Structural Effects in Benzonitrile Monolayers with Tuned Dipole Moments by Differently Positioned Fluorine Atoms. *ACS Appl. Mater. Interfaces* **2020**, *12*, 39859−39869.

(34) Wächter, T.; Scheetz, K. J.; Spaeth, A. D.; Barybin, M. V.; Zharnikov, M. Dynamics of Electron Transfer in Azulene-Based Self-Assembled Monolayers. *J. Phys. Chem. C* **2017**, *121*, 13777−13785.

(35) Ossowski, J.; Wächter, T.; Silies, L.; Kind, M.; Noworolska, A.; Blobner, F.; Gnatek, D.; Rysz, J.; Bolte, M.; Feulner, P.; et al. Thiolate versus Selenolate: Structure, Stability, and Charge Transfer Properties. *ACS Nano* **2015**, *9*, 4508−4526.

(36) Gibson, A. J.; Temperton, R. H.; Handrup, K.; O'Shea, J. N. Resonant Core Spectroscopies of the Charge Transfer Interactions between C60 and the Surfaces of Au(111), Ag(111), Cu(111) and Pt(111). *Surf. Sci.* **2017**, *657*, 69−78.

(37) Braun, S.; Salaneck, W. R.; Fahlman, M. Energy-Level Alignment at Organic/Metal and Organic/Organic Interfaces. *Adv. Mater.* **2009**, *21*, 1450−1472.

(38) Ko, C.-H.; Huang, M.-J.; Fu, M.-D.; Chen, C. Superior Contact for Single-Molecule Conductance: Electronic Coupling of Thiolate and Isothiocyanate on Pt, Pd, and Au. *J. Am. Chem. Soc.* **2010**, *132*, 756−764.

(39) Heimel, G.; Romaner, L.; Zojer, E.; Brédas, J.-L. Toward Control of the Metal−Organic Interfacial Electronic Structure in Molecular Electronics: A First-Principles Study on Self-Assembled Monolayers of π-Conjugated Molecules on Noble Metals. *Nano Lett.* **2007**, *7*, 932−940.

(40) Fenwick, O.; van Dyck, C.; Murugavel, K.; Cornil, D.; Reinders, F.; Haar, S.; Mayor, M.; Cornil, J.; Samorì, P. Modulating the Charge Injection in Organic Field-Effect Transistors: Fluorinated Oligophenyl Self-Assembled Monolayers for High Work Function Electrodes. *J. Mater. Chem. C* **2015**, *3*, 3007−3015.

(41) Xie, Z.; Bâldea, I.; Frisbie, C. D. Determination of Energy-Level Alignment in Molecular Tunnel Junctions by Transport and Spectroscopy: Self-Consistency for the Case of Oligophenylene Thiols and Dithiols on Ag, Au, and Pt Electrodes. *J. Am. Chem. Soc.* **2019**, *141*, 3670−3681.

(42) Xie, Z.; Bâldea, I.; Frisbie, C. D. Energy Level Alignment in Molecular Tunnel Junctions by Transport and Spectroscopy: Self-Consistency for the Case of Alkyl Thiols and Dithiols on Ag, Au, and Pt Electrodes. *J. Am. Chem. Soc.* **2019**, *141*, 18182−18192.

(43) Smith, C. E.; Xie, Z.; Bâldea, I.; Frisbie, C. D. Work Function and Temperature Dependence of Electron Tunneling through an N-Type Perylene Diimide Molecular Junction with Isocyanide Surface Linkers. *Nanoscale* **2018**, *10*, 964−975.

(44) Hamoudi, H.; Neppl, S.; Kao, P.; Schüpbach, B.; Feulner, P.; Terfort, A.; Allara, D.; Zharnikov, M. Orbital-Dependent Charge Transfer Dynamics in Conjugated Self-Assembled Monolayers. *Phys. Rev. Lett.* **2011**, *107*, 027801.

(45) Yuan, L.; Nerngchamnong, N.; Cao, L.; Hamoudi, H.; del Barco, E.; Roemer, M.; Sriramula, R. K.; Thompson, D.; Nijhuis, C. A. Controlling the Direction of Rectification in a Molecular Diode. *Nat. Commun.* **2015**, *6*, 6324.

(46) Rusu, P. C.; Brocks, G. Work Functions of Self-Assembled Monolayers on Metal Surfaces by First-Principles Calculations. *Phys. Rev. B* **2006**, *74*, 073414.

(47) Du, W.; Han, Y.; Hu, H.; Chu, H.-S.; Annadata, H. V.; Wang, T.; Tomczak, N.; Nijhuis, C. A. Directional Excitation of Surface Plasmon Polaritons via Molecular Through-Bond Tunneling across Double-Barrier Tunnel Junctions. *Nano Lett.* **2019**, *19*, 4634−4640.

(48) Carlotti, M.; Degen, M.; Zhang, Y.; Chiechi, R. C. Pronounced Environmental Effects on Injection Currents in EGaIn Tunneling Junctions Comprising Self-Assembled Monolayers. *J. Phys. Chem. C* **2016**, *120*, 20437−20445.

(49) Smith, C. E.; Odoh, S. O.; Ghosh, S.; Gagliardi, L.; Cramer, C. J.; Frisbie, C. D. Length-Dependent Nanotransport and Charge Hopping Bottlenecks in Long Thiophene-Containing π-Conjugated Molecular Wires. *J. Am. Chem. Soc.* **2015**, *137*, 15732−15741.

(50) Jiang, L.; Yuan, L.; Cao, L.; Nijhuis, C. A. Controlling Leakage Currents: The Role of the Binding Group and Purity of the Precursors for Self-Assembled Monolayers in the Performance of Molecular Diodes. *J. Am. Chem. Soc.* **2014**, *136*, 1982−1991.

(51) van Dyck, C.; Geskin, V.; Cornil, J. Fermi Level Pinning and Orbital Polarization Effects in Molecular Junctions: The Role of Metal Induced Gap States. *Adv. Funct. Mater.* **2014**, *24*, 6154−6165.

(52) Koch, N.; Heimel, G.; Wu, J.; Zojer, E.; Johnson, R. L.; Brédas, J.-L.; Müllen, K.; Rabe, J. P. Influence of Molecular Conformation on Organic/Metal Interface Energetics. *Chem. Phys. Lett.* **2005**, *413*, 390−395.

(53) Helander, M. G.; Greiner, M. T.; Wang, Z. B.; Lu, Z. H. Effect of Electrostatic Screening on Apparent Shifts in Photoemission Spectra near Metal/Organic Interfaces. *Phys. Rev. B* **2010**, *81*, 153308.

(54) Tong, Y.; Berdiyorov, G. R.; Sinopoli, A.; Madjet, M. E.; Esaulov, V. A.; Hamoudi, H. An Estimation on the Mechanical Stabilities of SAMs by Low Energy Ar+ Cluster Ion Collision. *Sci. Rep.* **2021**, *11*, 12772.

(55) Fadley, C. S.; Shirley, D. A. Electronic Densities of States from X-Ray Photoelectron Spectroscopy. *J. Res. Natl. Bur. Stand. A Phys. Chem.* **1970**, *74A*, 543−558.

(56) Cao, L.; Yuan, L.; Yang, M.; Nerngchamnong, N.; Thompson, D.; Yu, X.; Qi, D.-C.; Nijhuis, C. A. The Supramolecular Structure and van Der Waals Interactions Affect the Electronic Structure of Ferrocenyl-Alkanethiolate SAMs on Gold and Silver Electrodes. *Nano. Adv.* **2019**, *1*, 1991−2002.

(57) Cao, L.; Yang, M.; Yuan, L.; Nerngchamnong, N.; Feng, Y.-P.; Wee, A. T. S.; Qi, D.-C.; Nijhuis, C. A. Orbital Dependent Ultrafast Charge Transfer Dynamics of Ferrocenyl-Functionalized SAMs on Gold Studied by Core-Hole Clock Spectroscopy. *J. Phys.: Condens. Matter* **2016**, *28*, 094006.

(58) Zhang, J.; Hong, H.; Zhang, J.; Fu, H.; You, P.; Lischner, J.; Liu, K.; Kaxiras, E.; Meng, S. New Pathway for Hot Electron Relaxation in Two-Dimensional Heterostructures. *Nano Lett.* **2018**, *18*, 6057−6063.

(59) Wächter, T.; Tröster, A.; Hock, S.; Terfort, A.; Zharnikov, M. Dynamics of Electron Transfer in Self-Assembled Monolayers with Acene Backbone. *J. Phys. Chem. C* **2018**, *122*, 4105−4115.

(60) Salomon, A.; Cahen, D.; Lindsay, S.; Tomfohr, J.; Engelkes, V. B.; Frisbie, C. D. Comparison of Electronic Transport Measurements on Organic Molecules. *Adv. Mater.* **2003**, *15*, 1881−1890.

(61) Akkerman, H. B.; de Boer, B. Electrical Conduction through Single Molecules and Self-Assembled Monolayers. *J. Phys.: Condens. Matter* **2008**, *20*, 013001.

(62) Zharnikov, M. Probing Charge Transfer Dynamics in Self-Assembled Monolayers by Core Hole Clock Approach. *J. Electron Spectrosc. Relat. Phenom.* **2015**, *200*, 160−173.

(63) Ishii, H.; Sugiyama, K.; Ito, E.; Seki, K. Energy Level Alignment and Interfacial Electronic Structures at Organic/Metal and Organic/Organic Interfaces. *Adv. Mater.* **1999**, *11*, 605−625.

(64) Meyer, D.; Schäfer, T.; Schulz, P.; Jung, S.; Rittich, J.; Mokros, D.; Segger, I.; Maercks, F.; Effertz, C.; Mazzarello, R.; et al. Dithiocarbamate Self-Assembled Monolayers as Efficient Surface Modifiers for Low Work Function Noble Metals. *Langmuir* **2016**, *32*, 8812−8817.

(65) Kim, B.; Choi, S. H.; Zhu, X.-Y.; Frisbie, C. D. Molecular Tunnel Junctions Based on $\pi$-Conjugated Oligoacene Thiols and Dithiols between Ag, Au, and Pt Contacts: Effect of Surface Linking Group and Metal Work Function. *J. Am. Chem. Soc.* **2011**, *133*, 19864−19877.

(66) Gu, M.-W.; Peng, H. H.; Chen, I.-W. P.; Chen, C. Tuning Surface d Bands with Bimetallic Electrodes to Facilitate Electron Transport across Molecular Junctions. *Nat. Mater.* **2021**, *20*, 658−664.